Ceramics International 49 (2023) 37475–37485

Contents lists available at ScienceDirect

Ceramics International

journal homepage: www.elsevier.com/locate/ceramint

Effect of h-BN nanoparticles incorporation on the anti-corrosion and anti-wear properties of micro-arc oxidation coatings on 2024 aluminum alloy

Yixiong Gao [a], Shu Xiao [a,*], Hao Wu [b,**], Chunming Wu [c], Guohua Chen [a], Yansheng Yin [b], Paul K. Chu [d]

[a] School of Mechanical & Automotive Engineering, South China University of Technology, Guangzhou, 510641, China
[b] Guangdong Key Laboratory of Materials and Equipment in Harsh Marine Environment, School of Naval Architecture and Ocean Engineering, Guangzhou Maritime University, Guangzhou, 510725, China
[c] Guangdong Midea Precision Mold Technology Co., Ltd, Guangzhou, China
[d] Department of Physics, Department of Materials Science and Engineering, Department of Biomedical Engineering, City University of Hong Kong, Tat Chee Avenue, Kowloon, Hong Kong, China

ARTICLE INFO

Handling Editor: Dr P. Vincenzini

Keywords:
Hexagonal boron nitride
Micro-arc oxidation
Electrochemical properties
Self-lubrication

ABSTRACT

Micro-arc oxidation (MAO) coatings are recognized for their protective capabilities, yet their inherent porosity and defects limit broader applications. In this study, we aimed to rectify these limitations and enhance their performance by integrating hexagonal boron nitride (h-BN) nanoparticles into the MAO coatings. This work investigates the influence of h-BN concentration on the structure and properties of MAO coatings on 2024 aluminum alloy substrate. The results indicate that h-BN integration diminishes porosity and roughness, while improving hardness, adhesion, and corrosion and wear resistance. The corrosion current density (I_{corr}) of the most effective composite coatings is approximately 1% of the 2024 aluminum alloy substrate and 10% of undoped MAO coatings. Wear tests demonstrate the significant self-lubricating effect of the h-BN distributed in the coating, with the coefficient of friction (COF) of the most abrasion-resistant coating after h-BN doping being 67% of the undoped coating. During MAO, h-BN is uniformly incorporated into the coatings via diffusion and electrophoretic migration. The two-dimensional structure of h-BN in the coatings effectively blocks micro-defects, delays corrosive substance penetration, and enables self-lubrication. Conversely, excessive h-BN concentrations can instigate agglomeration and performance degradation. Optimum corrosion resistance is achieved with an h-BN concentration of 2.5 g/L, while the best wear resistance is attained at 10 g/L. The study suggests that h-BN-doped MAO coatings present substantial potential for applications necessitating high corrosion and wear resistance in aluminum alloys.

1. Introduction

Due to its low density, high strength-to-weight ratio, good mechanical properties and exceptional formability, the 2024 aluminum alloy is extensively employed in the aerospace and automotive industries [1]. However, its susceptibility to corrosion and wear hinders its broader application, particularly in harsh environments. Thus, developing advanced protective coatings is of paramount importance for enhancing the corrosion resistance and wear properties of 2024 alloys [2]. Micro-arc oxidation (MAO) which is an efficient and pollution-free method commonly used to prepare hard and adherent ceramic coatings on valve metals to improve corrosion resistance [3]. This method offers several advantages, including the in situ formation of thick, hard, and dense coatings with good adhesion to the substrate. However, one of the main drawbacks of MAO coatings is the presence of defects such as microporous microcracks, which can compromise their protective abilities [4]. Researchers have investigated various strategies, including polymer sealing [5], physical vapor deposition (PVD) [6], and electrolytic deposition [7] to improve the performance of MAO coatings. Nevertheless, these approaches often involve high costs and complex

* Corresponding author.
** Corresponding author.
E-mail addresses: xiaos@scut.edu.cn (S. Xiao), haowu.academic@gmail.com (H. Wu).

https://doi.org/10.1016/j.ceramint.2023.09.074
Received 30 August 2023; Accepted 8 September 2023
Available online 9 September 2023

preparation procedures, limiting their widespread application.

The incorporation of inert inorganic particles into MAO coatings has emerged as a research focus [8] repair defects and improve compactness and other properties [9]. For example, ZrO_2 [10], SiO_2 [11], ZnO [12], and TiO_2 [13] particles have been added to the electrolytes used in MAO. In this regard, two-dimensional (2D) layered materials have been proposed to minimize corrosion channels [14]. Xi et al. [15] have prepared MAO with two-dimensional sericite microplates to improve the corrosion and wear resistance of coatings. Chen et al. [16] have added an appropriate concentration of graphene oxide (GO) to the electrolyte to reduce the porosity and improve the corrosion resistance of the coatings. However, two-dimensional materials like GO and MXene are challenging to use widely due to their high preparation costs. Additionally, these two-dimensional materials, when doped into the coating and in contact with the base metal, are prone to galvanic corrosion due to their good conductivity, thus promoting corrosion and dissolution of the coating [17].

Hexagonal boron nitride (h-BN) has a melting point of nearly 3000 °C. Nitrogen and boron atoms form a hexagonal lattice that stacks to generate a crystalline structure [18]. Moreover, the flake structure of h-BN yields excellent physical barrier effects and self-lubrication [19]. h-BN exhibits good electrical insulation and extremely stable chemical properties, being insoluble in inorganic acids and water, as well as non-toxic and environmentally friendly [20]. This paper studies the effects of h-BN (1 μm) particles on the composition and structure of MAO coatings. Corrosion tests and friction tests are conducted on the prepared samples and related mechanisms are discussed.

2. Materials and methods

2.1. Preparation of MAO coatings

The MAO coatings were prepared on the 2024 aluminum alloy (40 mm × 25 mm × 2 mm). The substrate was polished with carbide paper, cleaned and dried at room temperature. 15 g/L Na_2SiO_3 and 10 g/L $(NaPO_3)_6$ in deionized water were used as the electrolyte. The h-BN (New Material Technology Ltd., Jiangsu) particles with different particle sizes and concentrations were mixed into the electrolyte to produce samples designated as MAO-0, MAO-2.5, MAO-5, MAO-10, MAO-15, where the number indicates the concentration of hexagonal boron nitride in the electrolyte. Before the MAO process, the electrolyte was stirred (1500 rad/min) and sonicated for 30 min to ensure even dispersion of h-BN flakes.

An 11 kW bipolar micro-arc oxidation power supply (Plasma Technol. Ltd., Hong Kong) was used for the MAO experiments, with the sample acting as the anode and a stainless-steel container serving as the cathode. The power supply output density was a constant positive current of 50 mA/cm^2. The frequency and duty cycle were set at 200 Hz and 30%, respectively. The MAO process was performed for 10 min for each sample.

2.2. Composition and structural characterization

Scanning electron microscopy (SEM, Carl Zeiss, SUPRA® 55) and energy-dispersive X-ray spectroscopy (EDS) were employed to analyze the morphology, structure, and elemental distribution of the coatings. The composition was examined using Grazing Incidence X-ray Diffraction (GIXRD) (Rigaku SmartLab) at a grazing incidence angle of 1° in the 2θ range of 10°–90°. The bonding state of h-BN in the coating was determined in situ by X-ray Photoelectron Spectroscopy (XPS) (Axis Ultra DLD). The effects of sodium hexametaphosphate and sodium silicate on the zeta potential of h-BN particles in the electrolyte were evaluated using a nanoparticle analyzer (HORIBA SZ-100Z).

2.3. Corrosion test

Electrochemical tests were conducted on an electrochemical workstation (Reference 600+, Gamry) with a standard three-electrode system. Potentiodynamic polarization tests were performed from −0.5 V to 0.5 V (vs. SCE) at a scanning rate of 1 mV/s after stabilization for 30 min in 3.5 wt% NaCl. Corrosion current densities (I_{corr}) and corrosion potentials (E_{corr}) were obtained using the Tafel extrapolation method. Electrochemical impedance spectroscopy (EIS) measurements were conducted using Gamry Instruments Framework electrochemical test software, with a frequency range of 0.1–1 × 10^5 Hz, an AC excitation signal amplitude of 20 mV, and a test duration of 2400 s. Both Tafel and EIS tests were repeated at least four times to ensure data reproducibility. The selection of electrochemical corrosion test parameters and methods followed those reported in previous work [15].

All samples for the immersion corrosion test were submerged in simulated seawater (3.5 wt% NaCl) for 14 days. Scanning electron microscopy (SEM) and 3D optical profilometry (Talysurf CLI 1000) were used to examine the surface morphology and corrosion products of the immersed samples.

2.4. Tribological testing

GCr15 steel balls (Ø = 6 mm) were employed in ball-on-disk type tribometer tests (MS ETC3000). The steel balls acted on the surface of the samples with a load of 2 N and a rate of 200 rad/min, with a friction radius of 3 mm and a test duration of 10 min. SEM and 3D optical profilometry (Talysurf CLI 1000) were utilized to investigate the wear track morphologies.

3. Results and discussion

3.1. Voltage-time response

Fig. 1 presents the voltage evolution during the MAO process. The voltage applied to the sample rapidly increases to approximately 300 V within the initial 50 s, corresponding to the anodizing stage where oxides form on the metal surface [21]. Beyond 50 s, the oxide film acts as a barrier, causing the voltage applied to the substrate to continually increase until the oxide film ultimately breaks down [22]. Notably, the terminal voltage experiences a slight increase as the h-BN concentration increases, which represents the maximum difference between the

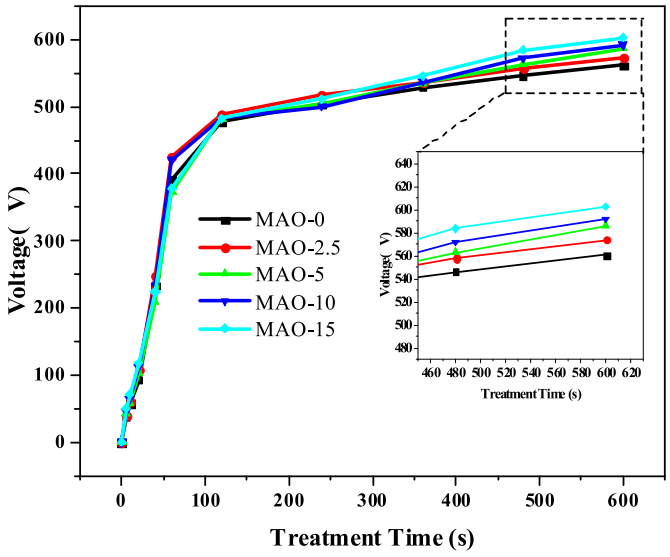

Fig. 1. Voltage-time response during the MAO process in the constant current mode.

voltage curves.

3.2. Composition and structure of the coatings

Fig. 2 displays the XRD and XPS spectra of the coatings. The broad peak between 25.66° and 27.28° in Fig. 2(a) originates from h-BN, confirming successful doping. As the h-BN concentration in the electrolyte increases, the diffraction peak intensity gradually rises. As depicted in Fig. 2(b), the peaks at 190.8 eV and 398.4 eV correspond to B and N, consistent with the XRD results. The B 1s and N 1s spectra are presented in Fig. 2(c and d) and 2(e-f), respectively. The two peaks at 190.8 eV and 192.5 eV signify B–N and B–O bonds, while B–N and N–H bonds are confirmed by the peaks at 398.4 eV and 400.4 eV in the N 1s spectrum. The majority of B and N atoms exist as BN within the MAO coatings. A minor portion of h-BN decomposes during the MAO discharge, as evidenced by the formation of new bonds with O and H [23].

Fig. 3 (a, c, e, g, i) display the SEM images of coatings at 30,000× magnification. The surfaces of all samples exhibit typical crater topography. Extremely high temperatures generated during the discharge process cause the alumina and aluminum metal substrates to melt or even vaporize and erupt outward. The molten mixture cools upon contact with the electrolyte and solidifies into a crater-like shape on the surface [3]. Fig. 3(c, e, g, i) illustrate the distribution of some h-BN particles. Fig. 3(b, d, f, h, j) present cross-sectional SEM images of MAO samples, revealing a wavy interfacial structure. However, the structure of the coatings does not change significantly after doping with h-BN. The EDS image of the cross-section demonstrates the distribution of Si and P in the coatings. Notably, the N and B elements are difficult to detect accurately with EDS due to their low atomic numbers and low X-ray emission energies.

Fig. 3(k) depicts the zeta potentials of h-BN in 15 g/L sodium silicate and 10 g/L sodium phosphate. Sodium silicate and sodium phosphate are the fundamental electrolyte components of this experimental system. As inorganic dispersants, sodium silicate and sodium phosphate adsorb onto h-BN. Comparatively, sodium phosphate modifies h-BN more effectively, and the zeta potential of −90 mV increases the migration efficiency of h-BN to the anode substrate in the electric field [24]. Sodium phosphate, a charge carrier with a small molecular weight, easily adsorbs onto particles, playing a role in electrostatic steric

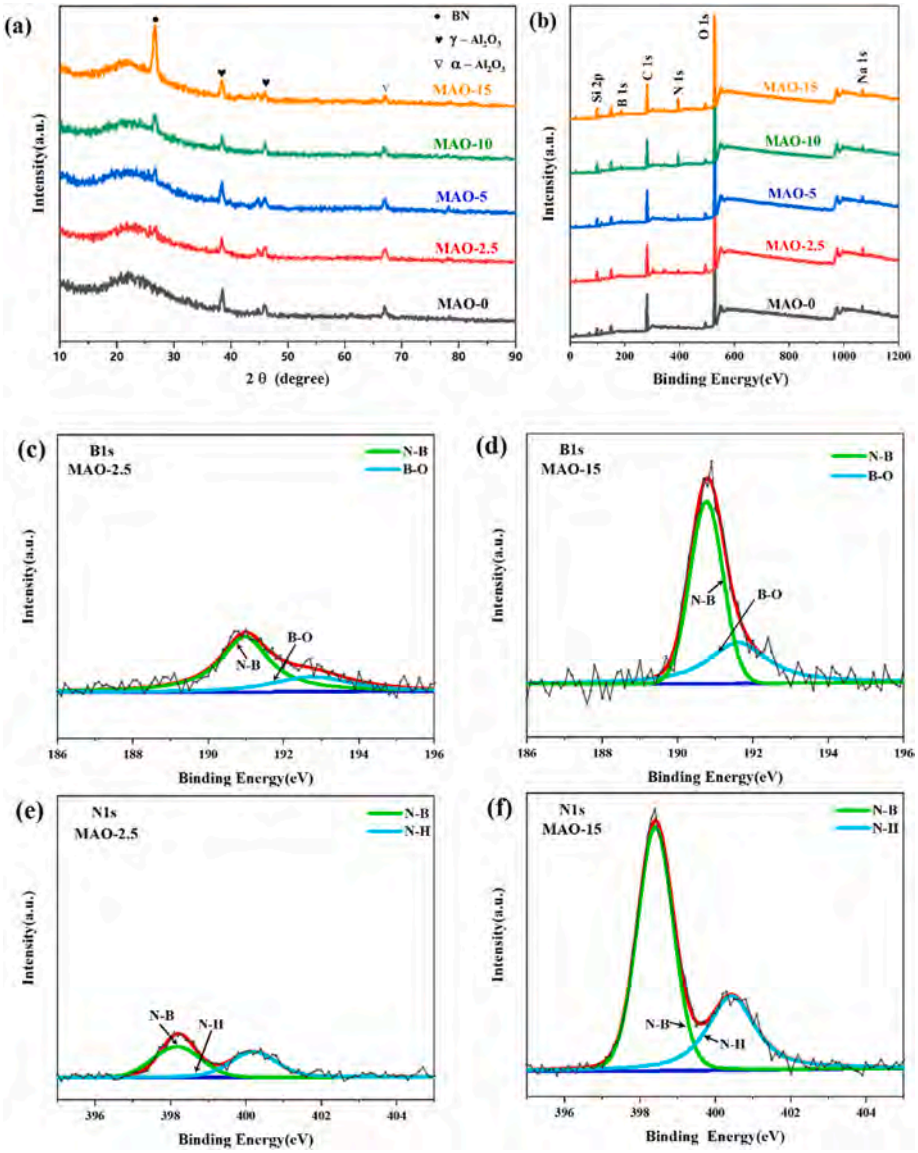

Fig. 2. XRD and XPS spectra of coatings; (a) GIXRD of five samples; (b) Full spectrum of X-ray photoelectron spectra of five samples; (c–f) High-resolution spectra of B1s and N1s in MAO-2.5 and MAO-15 coatings.

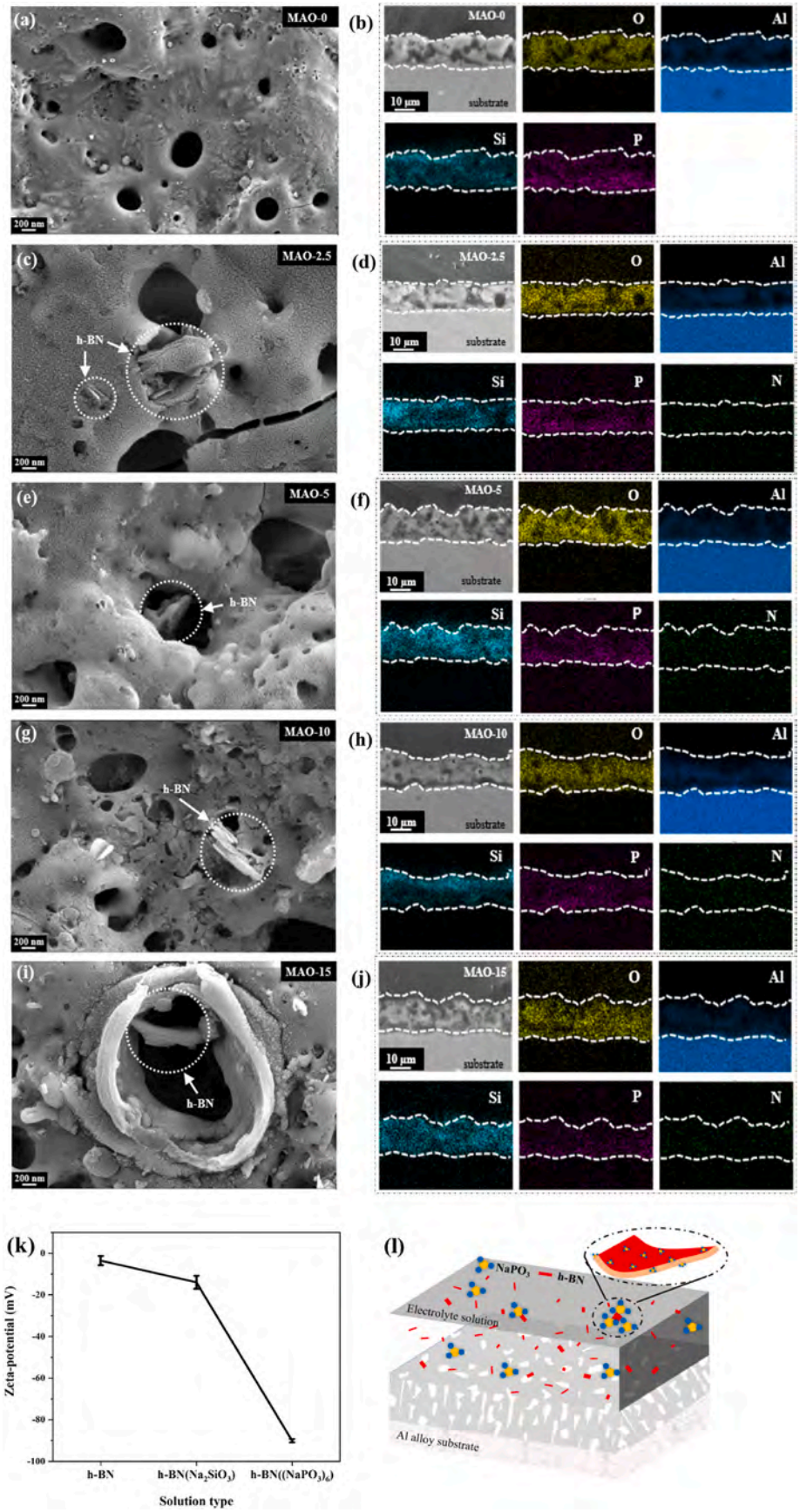

Fig. 3. SEM images of MAO-0, MAO-2.5, MAO-5, MAO-10, MAO-15. (a), (c), (e), (g), (i) are surface SEM images of samples. (b), (d), (f), (h), (j) are cross-sectional SEM images and EDS of samples. (k) Schematic diagram of h-BN doping into the coating; (l) Zeta potential of h-BN in different electrolyte compositions.

hindrance and dispersion. h-BN adsorbs sodium phosphate from the electrolyte, rendering h-BN negatively charged (Fig. 3l). The negatively charged h-BN moves towards the anode substrate under the electric field. Furthermore, the hydrodynamic effect of the mechanical stirring device in the electrolyte also promotes the doping of h-BN into the coating. Thus, the combined effect of electrophoresis and hydrodynamics enhances the integration of h-BN and coating.

Fig. 4(a–e) presents the results obtained after processing the surface SEM images of different samples using Image J software. The red area in the figure represents the location of pores. Due to the filling effect of h-BN, the porosity of h-BN-doped samples decreases in comparison to the porosity of MAO-0. Nonetheless, as indicated in Table 1, an increase in h-BN concentration results in more intense discharge, leading to a rise in porosity, thickness, and surface roughness of the sample [25]. In addition, the Vickers hardness of samples doped with BN is enhanced, with MAO-10 having the highest hardness. Consequently, the structure and composition of the sample undergo changes after doping with h-BN. The subsequent research will investigate the impact of these changes on the corrosion and wear resistance of the sample.

3.3. Electrochemical corrosion test results

To investigate the effect of different concentrations of h-BN on the corrosion behavior of coatings, preliminary work was conducted to examine the influence of h-BN particle size on the corrosion behavior. Fig. S1 and Table S1 reveal that samples doped with 1 μm h-BN particles exhibit the best corrosion resistance, regardless of whether the concentration of h-BN in the electrolyte is 5 g/L or 10 g/L. Thus, in subsequent experiments, 1 μm particles were used, and different concentrations of 0, 2.5, 5, 10, and 15 g/L were studied. Fig. 5(a) displays the Tafel polarization curves for each sample, and Table 2 and Fig. 5(b) show the corresponding corrosion potential (E_{corr}) and corrosion current density (I_{corr}). The MAO-2.5 sample displays the largest displacement on the forward potential in the Tafel curve. According to the fitted results in Table 2, the sample with the best corrosion resistance is MAO-2.5, as evidenced by an Icorr of 4.54×10^{-8} A cm^{-2}, which is approximately 1% of the 2024 aluminum alloy substrate and about 10% of the undoped h-BN coating [26]. Electrochemical impedance spectroscopy (EIS) curves of substrate, MAO-2.5, MAO-5, MAO-10, and MAO-15 are depicted in Fig. 3(c–e). The impedance modulus ($|Z|$) of the MAO-treated samples has been significantly increased in Fig. 3(c). The low-frequency impedance ($|Z|_{0.1Hz}$) in Fig. 3(c) is commonly used to evaluate the corrosion properties of the coatings and the MAO-2.5 shows the best impedance [27]. Fig. 5(e) shows significant differences in the impedance curves of each sample. The Nyquist curve of the MAO-2.5 sample exhibits the largest radian and the best corrosion resistance, consistent with the Tafel results. MAO-5 samples have the second-best corrosion resistance, while MAO-10 and MAO-15 exhibit slightly

Table 1
Average film thickness, surface roughness and Vickers hardness ($HV_{0.2}$) of each sample.

Sample	Average thickness (μm)	RMS (μm)	Vickers hardness ($HV_{0.2}$)
MAO-0	11.06	1.41	303 ± 17
MAO-2.5	12.26	1.48	326 ± 23
MAO-5	15.55	1.58	356 ± 19
MAO-10	17.98	1.92	412 ± 32
MAO-15	19.85	2.23	360 ± 27

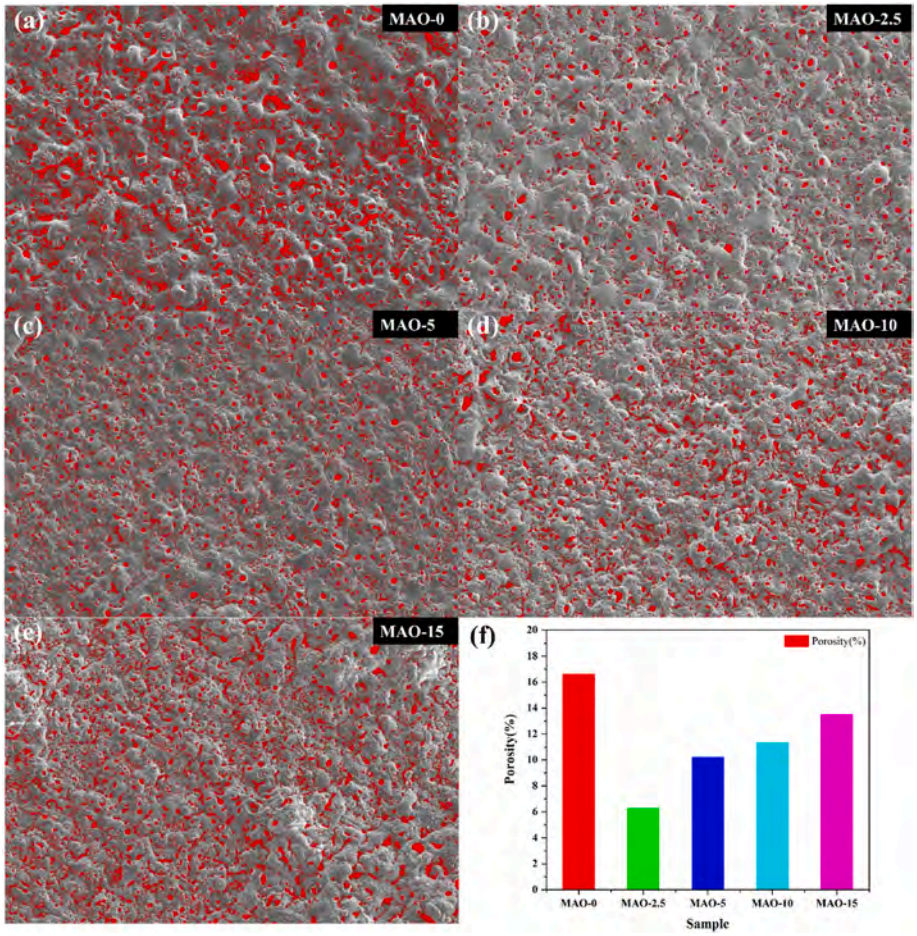

Fig. 4. (a–e) Surface pore distribution of samples; (f) Porosity of the samples.

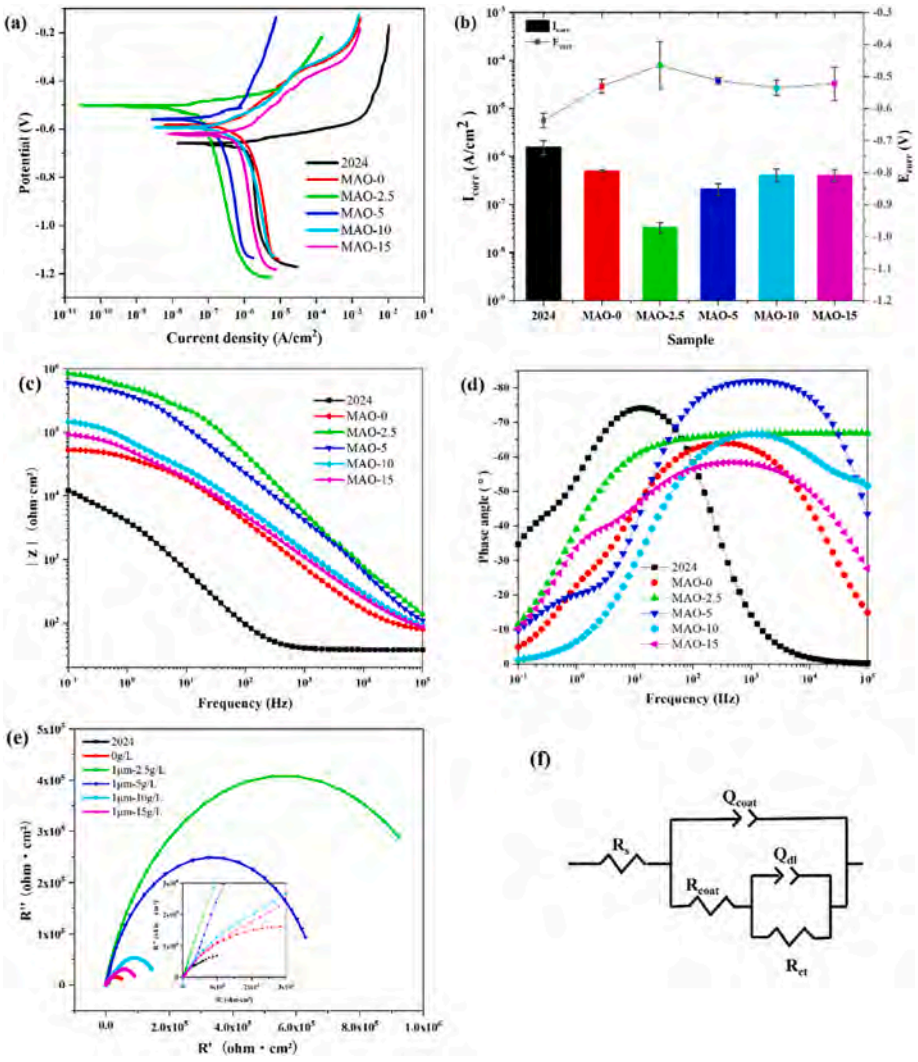

Fig. 5. (a) Tafel curves of the samples; (b) E_{corr} and I_{corr} from the polarization curves; (c–d) Bode diagrams; (e) Electrochemical impedance; (f) Equivalent circuit for the EIS data.

Table 2
Polarization analysis of the coatings after 30min soaking in 3.5 wt% NaCl.

Sample	E_{corr} (V vs. SCE)	I_{corr} (A·cm^{-2})
2024	−0.65	2.38×10^{-6}
MAO-0	−0.53	5.13×10^{-7}
MAO-2.5	−0.49	4.54×10^{-8}
MAO-5	−0.51	1.28×10^{-7}
MAO-10	−0.55	4.46×10^{-7}
MAO-15	−0.60	5.52×10^{-7}

better corrosion resistance than samples without h-BN and substrate, but still display the worst corrosion resistance among all samples.

The equivalent circuit R (Q (R (QR))) in Fig. 5(f) was used to fit the EIS data. The polarization resistance (R_p) is obtained by summing R_{coat} and R_{ct}, R_s represents the circuit resistance and electrolyte resistance, R_{coat} is the film resistance, R_{ct} denotes the charge transfer resistance, Q_{coat} is the coating capacitance, and Q_{dl} represents the double-layer capacitance [28]. As shown in Table 3, the R_p of MAO-2.5 is 100 times larger than that of substrates and MAO-0 and 10 times greater than that of MAO-10 and MAO-15, providing evidence that MAO-2.5 has the best corrosion resistance [29] followed by MAO-5. The samples with smaller R_p are MAO-10 and MAO-15, but R_p of these two samples are still higher than those of the samples without h-BN doping. In comparison, the 2024 substrate has the smallest R_p indicating the worst corrosion resistance. The results of the equivalent circuit fitting are consistent with the EIS and Tafel results.

Table 3
EIS data fitting results.

Sample	R_s (Ohm·cm^2)	Q_{coat} (Ohm^{-2}·cm^{-2}·S^{-n})	n_1	R_{coat} (Ohm·cm^2)	Q_{dl}	n_2	R_{ct} (Ohm·cm^2)
2024	37.37	3.402×10^{-5}	0.9141	7106	1.197×10^{-4}	0.842	1.332×10^{-4}
MAO-0	15.73	2.792×10^{-6}	0.6359	284.2	1.218×10^{-7}	1	5.514×10^{-4}
MAO-2.5	17.34	3.898×10^{-7}	0.7593	722.6	8.342×10^{-8}	0.9432	1.134×10^{-6}
MAO-5	17.81	2.540×10^{-7}	0.7731	9970	1.041×10^{-7}	0.8932	6.637×10^{-5}
MAO-10	134.9	6.088×10^{-7}	0.7638	5.075×10^{-4}	3.194×10^{-6}	0.8	1.241×10^{-5}
MAO-15	54.78	2.377×10^{-6}	0.6835	5.53×10^{-4}	3.212×10^{-6}	0.936	4.688×10^{-4}

3.4. Simulated seawater immersion testing

Fig. 6(a) depicts photographs of each sample after being immersed continuously in simulated seawater for varying durations. After 3 days, the bare 2024 aluminum alloy shows evident discoloration and corrosion damage. After 14 days, the corroded area on the undoped h-BN sample and MAO-15 is the largest. Conversely, the surface of MAO-2.5 rarely shows signs of corrosion and peeling. Fig. 6(b) displays the 3D morphology of 500 μm × 500 μm areas after immersion for 14 days. The figures reveal protrusions after corrosion, and the roughness RMS indicates that the sample without h-BN has the largest roughness. The roughness of the corroded area increases gradually with h-BN concentration, and the roughness RMS of MAO-2.5 after immersion is the smallest, corresponding to only 35% of that of MAO-0.

Fig. 7 shows SEM images and EDS results of each sample surface after 14 days of immersion. Fig. 7(a–j) show that MAO-0 and MAO-15 are almost completely covered by flocculent corrosion products, but no corrosion products are found from MAO-2.5. The amounts of corrosion products increase gradually with h-BN concentration in coatings. Fig. 7 (k) shows the elemental concentrations after immersion. The concentration of N increases with h-BN concentration but those of Al and O decrease. With the increase of h-BN concentration in electrolyte, h-BN is easy to form agglomeration on the substrate surface. The potential between the substrate and electrolyte increases as shown macroscopically by the voltage increase in Fig. 1. As the voltage goes up, the discharge on the surface becomes more intense [30], consequently producing thicker coatings and higher incorporation of h-BN from the electrolyte. Oxidation and melting of the aluminum alloy accelerate [31]. MAO coatings grow outward from the substrate. The closer to the coating surface, the Al element and Al_2O_3 from the substrate decrease, and the atomic concentrations of Al and O elements decrease.

The corrosion process of the aluminum alloy in the NaCl solution can be divided into the anode reaction and cathode reaction [32]. The anodic reaction involves the dissolution of aluminum to form aluminum ions and electrons (Eq. (1)) and aluminum ions hydrolyze in the solution to form corrosion products as shown by Eq. (2):

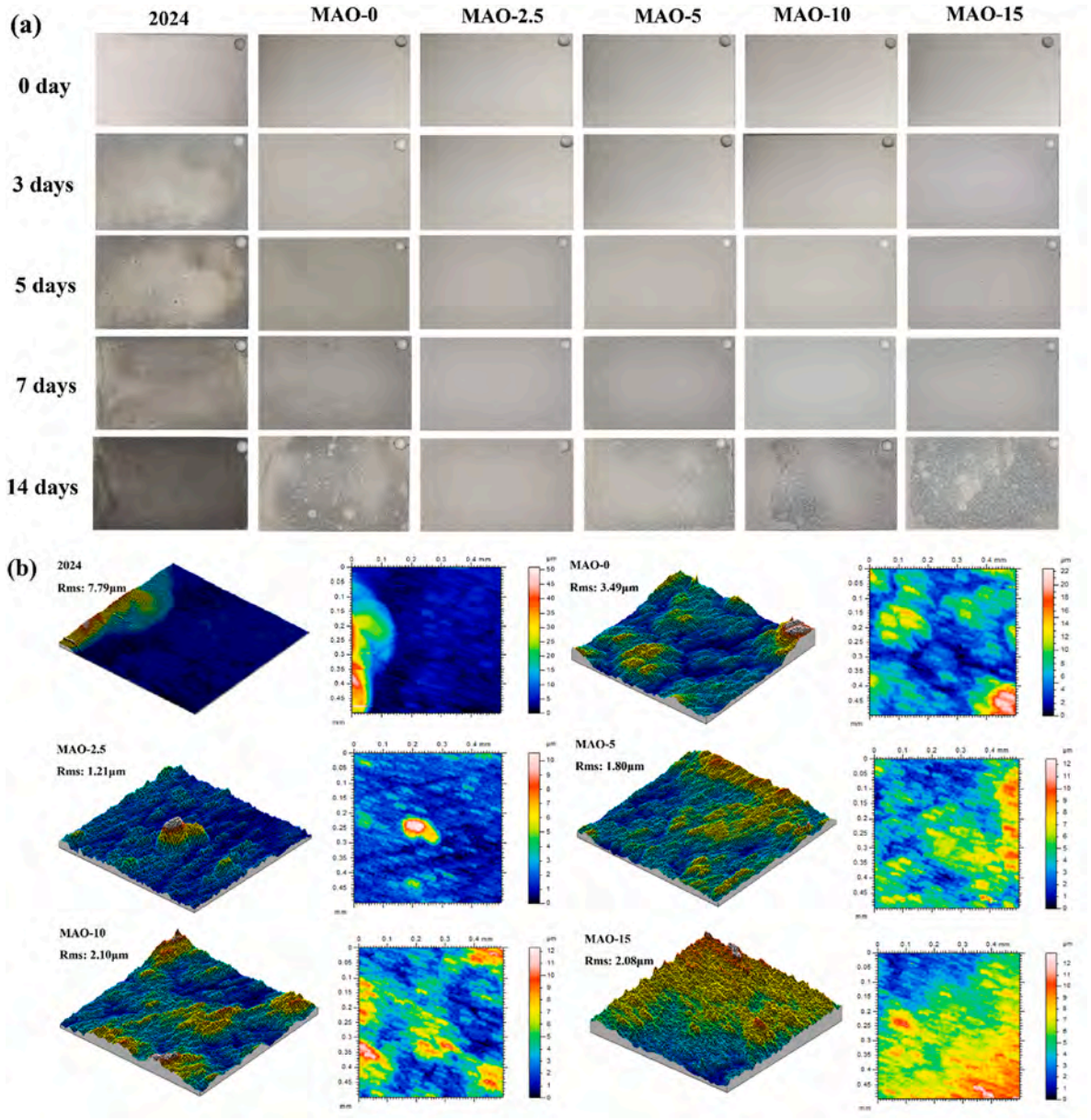

Fig. 6. (a) Snapshots from the 2024 substrate, MAO-0, MAO-2.5, MAO-5, MAO-10, MAO-15 during soaking; (b) 3D topography images of each sample after 14 days of immersion.

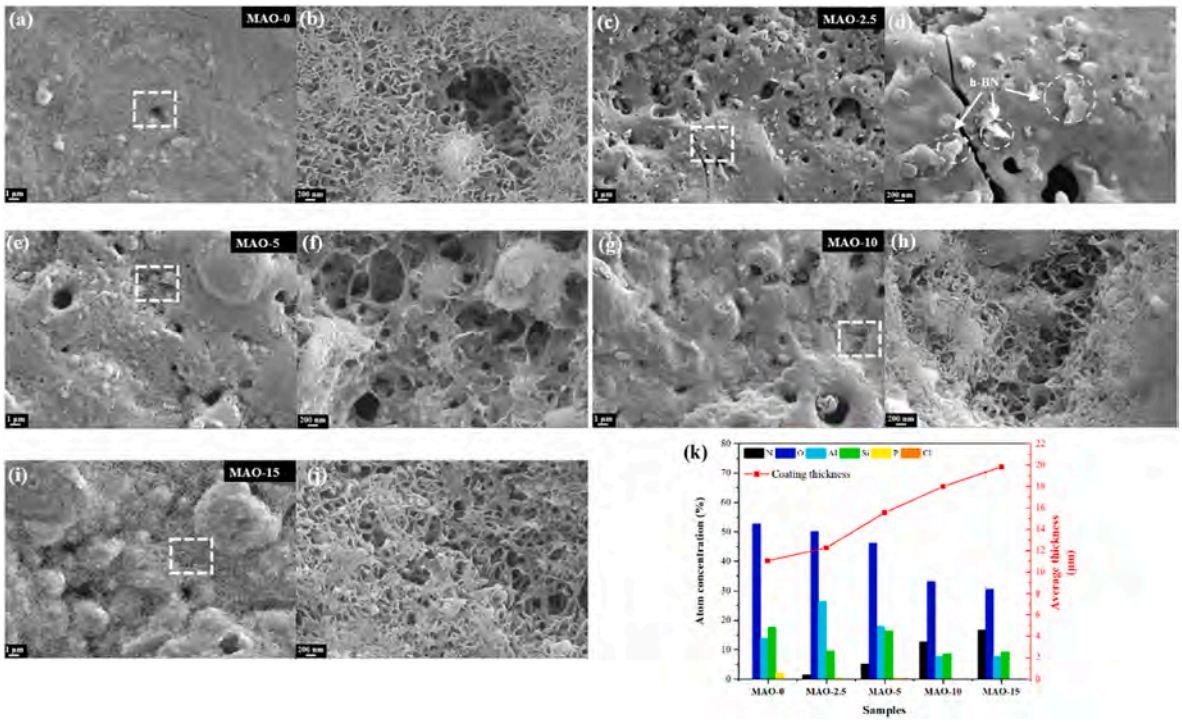

Fig. 7. (a–j) SEM images of each sample surface after 14 days of immersion, where figures (b), (d), (f), (h), (j) are enlarged views of the white box area in the figure (a), (c), (e), (g), (i); (k) The thickness of each coating before immersion corrosion and histogram of element concentration on sample surface after immersion.

$$Al \rightarrow Al^{3+} + 3e^{-} \quad (1)$$

$$Al^{3+} + nH_2O \rightarrow Al(OH)_n^{(3-n)} + nH^{+},\ n = 1,\ 2,\ \text{and}\ 3. \quad (2)$$

The electrons generated in reaction (1) participate in the cathode reaction which is mainly a hydrogen evolution reaction. As shown in Eq. (3):

$$2H_2O + 2e^{-} \rightarrow H_2 + 2OH^{-} \quad (3)$$

The corrosion products formed in reaction (2) can be converted into more stable oxides, as shown in Eq. (4):

$$2Al(OH)_3 \rightarrow Al_2O_3 + 3H_2O \quad (4)$$

Therefore, $Al(OH)_3$ and Al_2O_3 cover the surface to form a passivation layer. However, Cl^{-} can destroy the passivation layer via reactions (5), (6), and (7):

$$Al(OH)_3 + Cl^{-} \rightarrow Al(OH)_2Cl + OH^{-} \quad (5)$$

$$Al(OH)_2Cl + Cl^{-} \rightarrow Al(OH)Cl_2 + OH^{-} \quad (6)$$

$$Al(OH)Cl_2 + Cl^{-} \rightarrow AlCl_3 + OH^{-} \quad (7)$$

H^{+} in the solution reacts with A:

$$2Al + 6HCl \rightarrow 2AlCl_3 + 3H_2 \quad (8)$$

The corrosion product $AlCl_3$ undergoes hydrolysis again as shown in Eq. (2). Therefore, in the presence of Cl^{-}, the reactions are cyclical leading to continuous corrosion of aluminum. In particular, there is a difference in ion concentration between the pitting pit and the external solution, resulting in strong acidity in the pitting pit, which makes the corrosion of the passivation layer more serious [33].

3.5. Friction and wear test

Fig. 8(a) shows the trend of friction coefficient of different samples over time under dry friction conditions. The COF of the MAO-0 of about 0.6 is the largest among all samples. The COFs of MAO-2.5 and MAO-5 decrease to 0.5 and 0.45 respectively and a minimum of 0.4 is observed from MAO-10. When the concentration of h-BN is increased to 15 g/L, the COF of the sample goes up to about 0.6. Fig. 8(b) shows the 2D profiles of the abrasion marks. MAO-10 shows the smallest abrasion depth and MAO-0 the deepest. Table 4 compares the wear rates and MAO-10 has the smallest wear rate, which is 60% of that of MAO-2.5 and MAO-5. Fig. 8(c–q) shows the SEM and 3D images of the scratch. After samples are worn, the wear scar appears flaky and shows a tendency to delaminate. The MAO-0 and MAO-15 samples exhibit the largest peeling tendency, whereas MAO-5 and MAO-10 are less likely to come off.

3.6. Mechanism of action of h-BN

Fig. 9(a–c) depict the corrosion and wear behavior of coatings doped with h-BN. Without h-BN (Fig. 9(a)), corrosive media penetrates micropores and defects, causing damage to the substrate [34]. However, due to its large lateral and axial size ratio and layered structure, h-BN acts as an effective physical barrier, sealing micropores and cracks and making it difficult for corrosive media to diffuse (Fig. 9(b)). The insulating nature of h-BN also mitigates galvanic corrosion of aluminum, while its self-lubricating properties result in smaller COF in tribological tests [35]. Additionally, the large specific surface area of h-BN reduces contact between the steel ball and MAO coatings, as seen in Fig. 9(c) [36].

Nevertheless, the combination of h-BN with the coating does not always lead to improved performance. In this study, MAO-2.5 and MAO-10 MAO-2.5 and MAO-10 correspond to the lowest surface porosity and the highest Vickers hardness, and exhibit the best corrosion resistance and wear resistance, respectively. However, further increasing the concentration of h-BN led to a decrease in coating performance. For instance, increasing h-BN concentration resulted in greater surface porosity and lower Vickers hardness, as seen in Fig. 4 and Table 1, reducing the coating's corrosion and wear resistance. During MAO

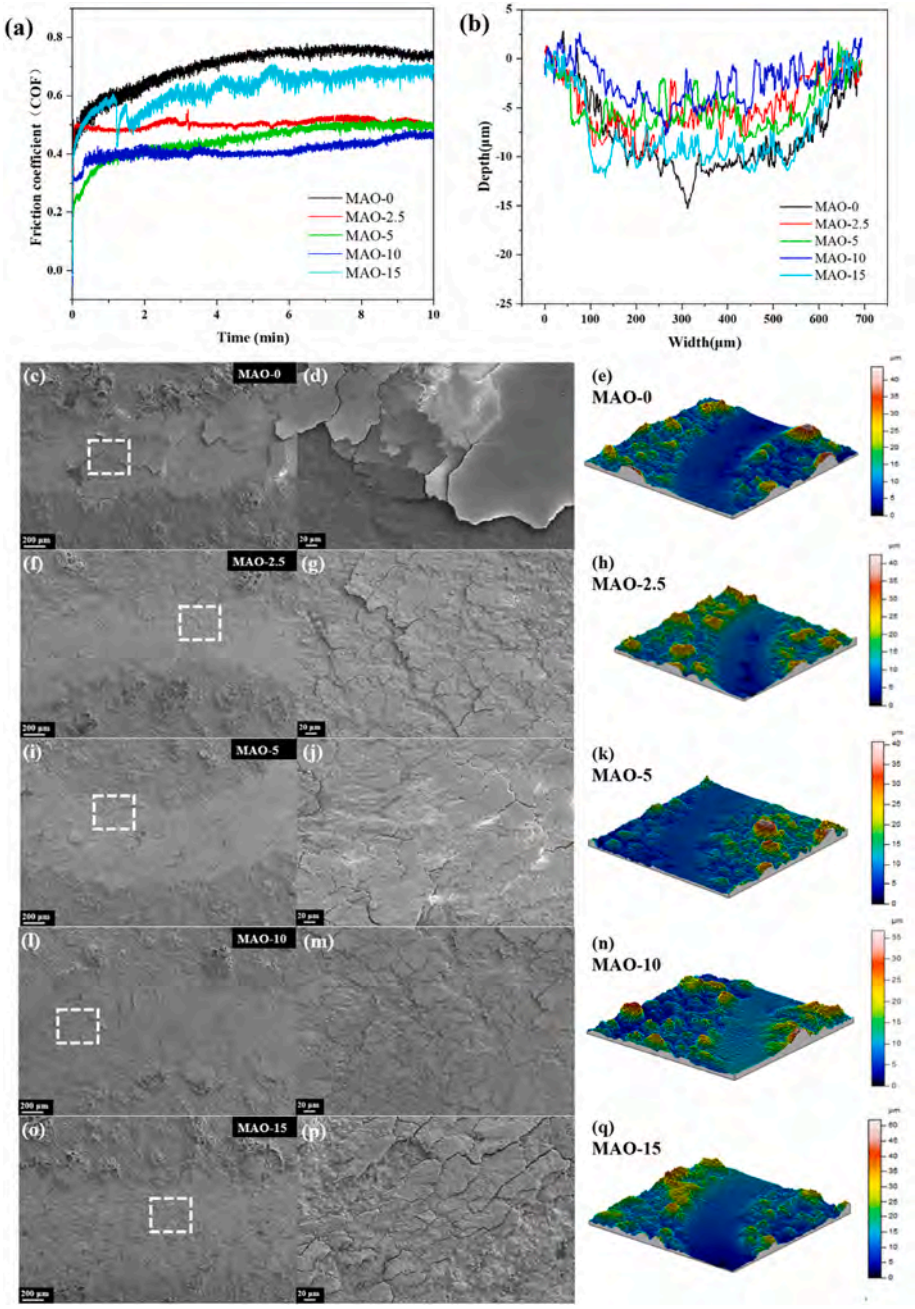

Fig. 8. (a) The trend of friction coefficient of different samples over time; (b) 2D profile; (c–q) SEM and 3D profile of sample wear scar, where figures (d), (g), (j), (m), (p) are enlarged views of the white box area in the figure (c), (f), (i), (l), (o).

Table 4
Wear rates of different samples calculated from the friction test.

Sample	MAO-0	MAO-2.5	MAO-5	MAO-10	MAO-15
Wear rate (mm^3/Nm)	1.29×10^{-3}	7.17×10^{-4}	7.11×10^{-4}	4.30×10^{-4}	1.00×10^{-3}

discharge, h-BN adsorbs onto the substrate, leading to more intense discharges and creating more discharge channels and microcracks. While a small amount of h-BN can block micro-defects and reduce corrosion, excessive h-BN concentration creates agglomerations that disrupt ceramic coating compactness, increase coating defects, and lead to spalling and higher friction coefficients [25,37]. Moreover, electrophoresis and hydrodynamic forces are not sufficient to evenly distribute high concentrations of h-BN, exacerbating agglomeration formation.

4. Conclusion

Hexagonal boron nitride (h-BN)-doped coatings are fabricated on aluminum via MAO, and their structure, phase composition, corrosion resistance, and tribological properties are investigated. The characterization results reveal that the incorporation of h-BN into MAO coatings significantly improved their corrosion and wear resistance. The incorporation of h-BN into MAO coatings significantly improved their corrosion and wear resistance. The best corrosion resistance was observed in coatings with h-BN concentrations of 2.5 g/L, while the best wear resistance was observed in coatings with h-BN concentrations of 10 g/L. However, increasing the h-BN concentration further deteriorated the coating's performance due to the formation of agglomerated h-

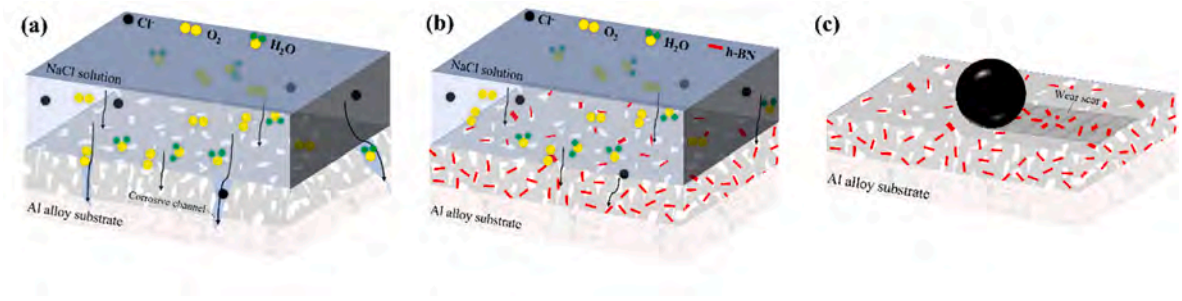

Fig. 9. (a–c) The corrosion and wear behavior of coatings after doping h-BN.

BN, which destroyed the compactness of the ceramic coating and increased coating defects, resulting in higher friction coefficients. The physical barrier and insulating properties of h-BN played a crucial role in improving the corrosion and wear resistance of the MAO coatings. Our findings provide important insights into the design and development of new and improved MAO coatings for applications of aluminum alloys in harsh environment.

Declaration of competing interest

The authors declare that they have no known competing financial interests or personal relationships that could have appeared to influence the work reported in this paper.

Acknowledgements

We acknowledge the financial support from National Natural Science Foundation of China (Nos. 52005187, 51905177, and 52071091, and 52375182), Natural Science Foundation of Guangdong Province (No.2023A1515012308), Open fund of Guangdong Provincial Key Laboratory of petrochemical equipment fault diagnosis (No. 91720202), City University of Hong Kong Donation Research Grant (DON-RMG 9229021), City University of Hong Kong Donation Grant (9220061), and City University of Hong Kong Strategic Research Grant (SRG) (No. 7005505).

Appendix A. Supplementary data

Supplementary data to this article can be found online at https://doi.org/10.1016/j.ceramint.2023.09.074.

References

[1] Y.F. Song, X.F. Ding, L.R. Xiao, X.J. Zhao, Z.Y. Cai, L. Guo, Y.W. Li, Z.Z. Zheng, Effects of two-stage aging on the dimensional stability of Al-Cu-Mg alloy, J. Alloys Compd. 701 (2017) 508–514.
[2] R.Y. Sun, Z. Li, J. Zhao, J.L. Mo, Y.J. Pan, D.B. Luo, Facile fabrication of durable superhydrophobic aluminum alloy surfaces by HS-WEDM and chemical modification, Nano 16 (2021).
[3] M. Kaseem, S. Fatimah, N. Nashrah, Y.G. Ko, Recent progress in surface modification of metals coated by plasma electrolytic oxidation: principle, structure, and performance, Prog. Mater. Sci. 117 (2021).
[4] W.B. Tu, Y.L. Cheng, X.Y. Wang, T.Y. Zhan, J.X. Han, Y.L. Cheng, Plasma electrolytic oxidation of AZ31 magnesium alloy in aluminate-tungstate electrolytes and the coating formation mechanism, J. Alloys Compd. 725 (2017) 199–216.
[5] H.B. Lee, H.H. Sheu, J.S. Jian, R.C. Hsiao, Study on the characteristics of MAO/polymer/Ni three-layer composite film formed on AZ31 magnesium alloy, Int. J. Electrochem. Sci. 16 (2021).
[6] S.L. Aktug, S. Durdu, S. Aktas, E. Yalcin, M. Usta, Surface and in vitro properties of Ag-deposited antibacterial and bioactive coatings on AZ31 Mg alloy, Surf. Coating. Technol. 375 (2019) 46–53.
[7] Y.M. Shangguan, L.N. Sun, P. Wan, L.L. Tan, C.Y. Wang, X.M. Fan, L. Qin, K. Yang, Comparison study of different coatings on degradation performance and cell response of Mg-Sr alloy, Mater. Sci. Eng., C 69 (2016) 95–107.
[8] Y. Yurekturk, F. Muhaffel, M. Baydogan, Characterization of micro arc oxidized 6082 aluminum alloy in an electrolyte containing carbon nanotubes, Surf. Coating. Technol. 269 (2015) 83–90.
[9] Z.D. Zhu, W.B. Tu, Y.L. Cheng, Y.L. Cheng, The formation of metallic W and amorphous phase in the plasma electrolytic oxidation coatings on an Al alloy from tungstate-containing electrolyte, Surf. Coating. Technol. 361 (2019) 176–187.
[10] W. Shao, C.C. Liu, Q.J. Wu, H.T. Li, L.A. Angurel, G.F. de la Fuente, B.L. Jiang, Comparison of in-situ oxidation behavior of Zr by micro-arc oxidation and selective laser melting, J. Eur. Ceram. Soc. 42 (2022) 6703–6712.
[11] X.P. Lu, C. Blawert, Y.D. Huang, H. Ovri, M.L. Zheludkevich, K.U. Kainer, Plasma electrolytic oxidation coatings on Mg alloy with addition of SiO2 particles, Electrochim. Acta 187 (2016) 20–33.
[12] Q. Huang, Z.Z. Wu, H. Wu, S.P. Ji, Z.Y. Ma, Z.C. Wu, P.H. Chen, J.Y. Zhu, R.K.Y. Fu, H. Lin, X.B. Tian, F. Pan, P.K. Chu, Corrosion behavior of ZnO-reinforced coating on aluminum alloy prepared by plasma electrolytic oxidation, Surf. Coating. Technol. 374 (2019) 1015–1023.
[13] B.S. Necula, I. Apachitei, F.D. Tichelaar, L.E. Fratila-Apachitei, J. Duszczyk, An electron microscopical study on the growth of TiO2-Ag antibacterial coatings on Ti6Al7Nb biomedical alloy, Acta Biomater. 7 (2011) 2751–2757.
[14] H. Yan, L. Zhang, H. Li, X.Q. Fan, M.H. Zhu, Towards high-performance additive of Ti3C2/graphene hybrid with a novel wrapping structure in epoxy coating, Carbon 157 (2020) 217–233.
[15] K. Xi, H. Wu, C.L. Zhou, Z.Y. Qi, K.L. Yang, R.K.Y. Fu, S. Xiao, G.S. Wu, K.J. Ding, G.H. Chen, P.K. Chu, Improved corrosion and wear resistance of micro-arc oxidation coatings on the 2024 aluminum alloy by incorporation of quasi-two-dimensional sericite microplates, Appl. Surf. Sci. 585 (2022).
[16] Q.Z. Chen, Z.Q. Jiang, S.G. Tang, W.B. Dong, Q. Tong, W.Z. Li, Influence of graphene particles on the micro-arc oxidation behaviors of 6063 aluminum alloy and the coating properties, Appl. Surf. Sci. 423 (2017) 939–950.
[17] C.L. Cui, A.T.O. Lim, J.X. Huang, A cautionary note on graphene anti-corrosion coatings, Nat. Nanotechnol. 12 (2017) 834–835.
[18] C.W. Lu, C.J. Wang, J.B. Gu, First-principles study of structural, elastic, thermodynamic, electronic and optical properties of cubic boron nitride and hexagonal boron nitride at high temperature and high pressure, Acta Phys. Sin. 68 (2019).
[19] X.H. Zhu, J.G. Fu, D.Q. Ma, C.S. Ma, Y.Y. Fu, Z.K. Zhang, Effect of nano h-BN particles on growth regularity and tribological behavior of PEO composite ceramic coating of ZL109 alloy, Sci. Rep. 12 (2022).
[20] D. Lee, S.H. Song, Ultra-thin ultraviolet cathodoluminescent device based on exfoliated hexagonal boron nitride, vol 7, pg 7831, RSC Adv. 7 (2017), 2017) 10815-10815.
[21] R.O. Hussein, X. Nie, D.O. Northwood, An investigation of ceramic coating growth mechanisms in plasma electrolytic oxidation (PEO) processing, Electrochim. Acta 112 (2013) 111–119.
[22] L.J. Zhu, X.X. Ke, J.W. Li, Y.F. Zhang, Z.H. Zhang, M.L. Sui, Growth mechanisms for initial stages of plasma electrolytic oxidation coating on Al, Surface. Interfac. 25 (2021).
[23] C.C. Huang, H.M. Li, S.Y. Lin, D.H. Li, Effect of different concentrations of nano-cubic boron nitride on the preparation of TiO2/Ti/Fe composite materials by thermal sprayed and Micro-Arc oxidation, Mater. Trans. 62 (2021) 1462–1470.
[24] S. Bhattacharjee, B.P. Singh, L. Besra, D.K. Sengupta, Performance evaluation of dispersants through streaming potential measurements, J. Dispersion Sci. Technol. 26 (2005) 365–370.
[25] W. Shang, Y.Y. Wang, Y.Q. Wen, X.Q. Zhan, D. Kong, Study on the properties of micro - arc oxidation self - assembled composite coatings on magnesium alloy, Int. J. Electrochem. Sci. 12 (2017) 11875–11891.
[26] Z.Q. Zhang, F. He, C.X. Huang, Z.K. Song, J.X. Yang, X.D. Wang, Effect of Fe3+ and F- on black micro-arc oxidation ceramic coating of magnesium alloy, Int. J. Appl. Ceram. Technol. 19 (2022) 2203–2212.
[27] P.F. Ji, K. Lu, W.D. Chen, M.L. Wang, Study on preparation of Micro-Arc oxidation film on TC4 alloy with titanium dioxide colloid in electrolyte, Coatings (2022) 12.
[28] Q.P. Tran, T.S. Chin, Y.C. Kuo, C.X. Jin, T. Trung, C.V. Tuan, D.Q. Dang, Diamond powder incorporated oxide layers formed on 6061 Al alloy by plasma electrolytic oxidation, J. Alloys Compd. 751 (2018) 289–298.
[29] Y.D. Liu, J. Zhao, X.Y. Yang, Y.H. Gu, Z.H. Yang, Local electrochemical corrosion performance of nano-SiC/MAO composite coating on 6061-Al alloy, Anti-corrosion Methods & Mater. 69 (2022) 592–602.
[30] X.P. Lu, M. Mohedano, C. Blawert, E. Matykina, R. Arrabal, K.U. Kainer, M. L. Zheludkevich, Plasma electrolytic oxidation coatings with particle additions - a review, Surf. Coating. Technol. 307 (2016) 1165–1182.

[31] P. Molaeipour, S.R. Allahkaram, S. Akbarzadeh, Corrosion Inhibition of Ti6Al4V Alloy by a Protective Plasma Electrolytic Oxidation Coating Modified with Boron Carbide Nanoparticles, Surface & Coatings Technology, 2022, p. 430.
[32] H. Yan, J.C. Wang, C. Meng, X. Wang, S.J. Song, X.Q. Fan, L. Zhang, H. Li, W. Li, M. H. Zhu, Towards long-term corrosion and wear protection of Al alloy: synergy of Ti3C2Tx flake and micro-arc oxidation coating, Corrosion Sci. 174 (2020).
[33] E. McCafferty, Sequence of steps in the pitting of aluminum by chloride ions, Corrosion Sci. 45 (2003) 1421–1438.
[34] P.C. Rice-Evans, I.J. Franco, Observation of a localised oscillatory mode of optical emission from an air plasma, J. Phys. D Appl. Phys. 13 (1980) 1079–1082.
[35] E. Kaplan, E.E. Sukuroglu, O. Cuvalci, Investigation of characterization and tribological behavior of composite oxide coatings doped with h-BN and graphite particles on ZA-27 alloy by micro-arc oxidation, J. Adhes. Sci. Technol. 35 (2021) 1305–1319.
[36] X.Y. Li, C.F. Dong, Q. Zhao, Y. Pang, F.S. Cheng, S.X. Wang, Characterization of microstructure and wear resistance of PEO coatings containing various microparticles on Ti6Al4V alloy, J. Mater. Eng. Perform. 27 (2018) 1642–1653.
[37] G.Q. Xu, X.K. Shen, Fabrication of SiO2 nanoparticles incorporated coating onto titanium substrates by the micro arc oxidation to improve the wear resistance, Surf. Coating. Technol. 364 (2019) 180–186.

Supplementary Materials

Effect of h-BN nanoparticles incorporation on the anti-corrosion and anti-wear properties of micro-arc oxidation coatings on 2024 aluminum alloy

Yixiong Gao [a], Shu Xiao [a*], Hao Wu [b*], Chunming Wu [c], Guohua Chen[a], Paul K. Chu [d]

[a] *School of Mechanical & Automotive Engineering, South China University of Technology, Guangzhou 510641, China*

[b] *Guangdong Key Laboratory of Materials and Equipment in Harsh Marine Environment, School of Naval Architecture and Ocean Engineering, Guangzhou Maritime University, Guangzhou 510725, China*

[c] *Guangdong Midea Precision Mold Technology Co., Ltd, Guangzhou, China*

[d] *Department of Physics, Department of Materials Science and Engineering, and Department of Biomedical Engineering, City University of Hong Kong, Tat Chee Avenue, Kowloon, Hong Kong, China*

** Corresponding author*

Table.S1. E_{corr} and I_{corr} of the different samples derived from the Tafel curves.

Sample	E_{corr} (V vs. SCE)	I_{corr} ($A \cdot cm^{-2}$)
2024	-0.63	1.21×10^{-6}
0g/L	-0.53	6.40×10^{-7}
100nm-5g/L	-0.61	4.14×10^{-7}
1μm-5g/L	-0.51	1.28×10^{-7}
3~5μm-5g/L	-0.56	2.52×10^{-7}
100nm-10g/L	-0.59	8.42×10^{-7}
1μm-10g/L	-0.55	4.46×10^{-7}
3~5μm-10g/L	-0.60	5.12×10^{-7}

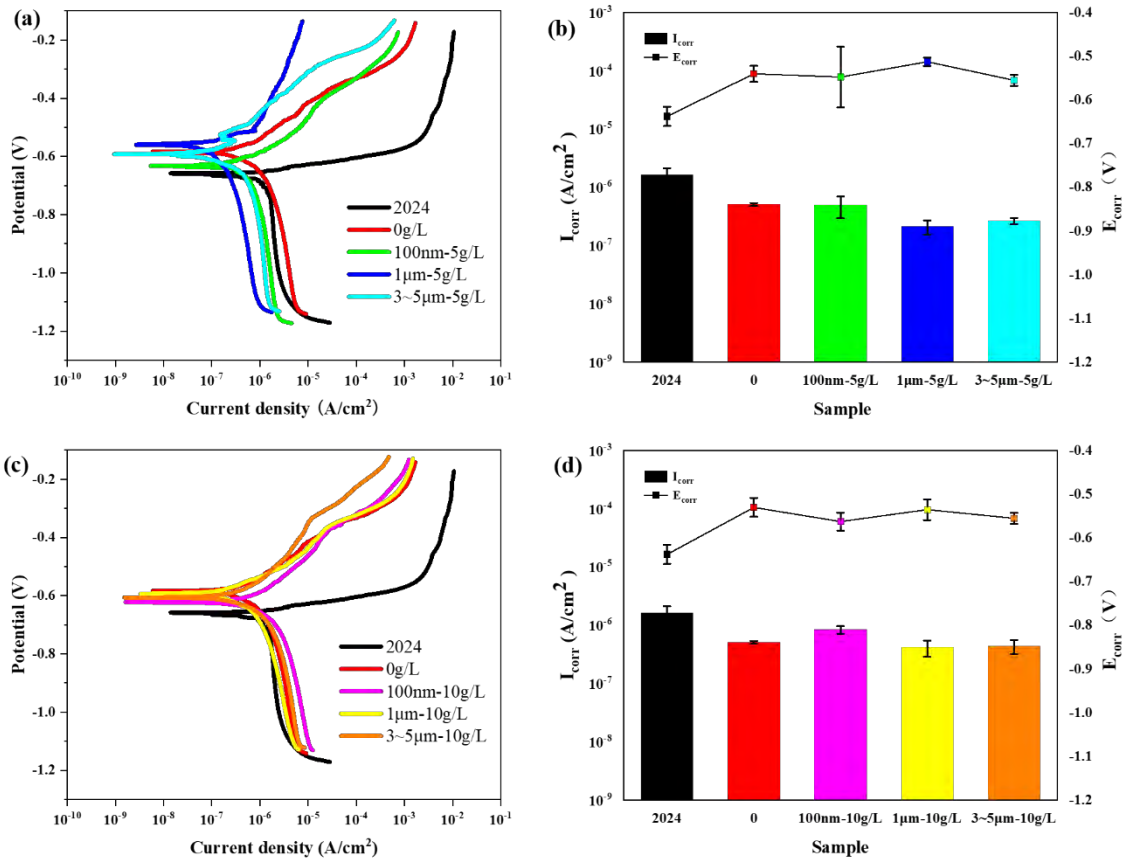

Fig. S1. (a) Tafel curve of samples prepared with three different particle sizes and the same concentration (5 g/L) of h-BN; (b) Corresponds to the E_{corr} and I_{corr} of each sample in (a); (c) Tafel curve of samples prepared from 2024 substrate and electrolyte with three different particle sizes and the same concentration (10g/L) of h-BN; (d) Corresponds to the E_{corr} and I_{corr} of each sample in (c).

Figures S1(a) and (c) show the potentiodynamic polarization (POL) curves of samples prepared with three particle sizes of h-BN. h-BN particles with different sizes and concentrations were mixed into the electrolyte and the samples were labeled as 0g/L, 100nm-5g/L, 100nm-10g/L, 1μm-5g/L, 1μm-10g/L, 3~5μm-5g/L, and 3~5μm-10g/L, where 100nm, 1μm, and 3~5μm represent the h-BN particle size and 0g/L and 5g/L represent the h-BN concentration. Table S1 lists the E_{corr} and I_{corr} of the Tafel curve. Figure S1(a) shows that the Tafel curves of the samples prepared with the same h-BN concentration (5 g/L) shift to the left. Among the three particle sizes, the curve of the 1μm-5g/L sample exhibits the largest positive and left shift, whereas E_{corr} is the largest and I_{corr} is the smallest. According to the fitted data, I_{corr} of the base treated by MAO decreases from 1.21×10^{-6} A · cm^{-2} to 6.4×10^{-7} A·cm^{-2} and the corrosion potentials increase from -0.63 V to -0.53 V. When 5 g/L h-BN is added to the electrolyte, the coating doped with 1 μm particles shows the best corrosion resistance among the 100 nm, 1 μm, and 3~5 um particle size samples. I_{corr} of the 1μm-5g/L sample is about 10% of the aluminum substrate and corresponds to 20% of the undoped h-BN sample. Figs. S1(c) and (d) show that the curve of the 1μm-10g/L sample still shows the largest positive and left shift as well as the biggest E_{corr} and smallest I_{corr}. Table 1 shows that I_{corr} of the 1μm-10g/L sample is 4.46×10^{-7} A·cm^{-2}. Fig. S1 and Table 1 indicate that for concentrations of 5 g/L or 10 g/L, the coating prepared with 1 μm h-BN has better anti-corrosion capability than the other three samples. Moreover, the improvement in the corrosion resistance observed from samples with 10 g/L h-BN is smaller than that of the sample prepared with 5 g/L h-BN.

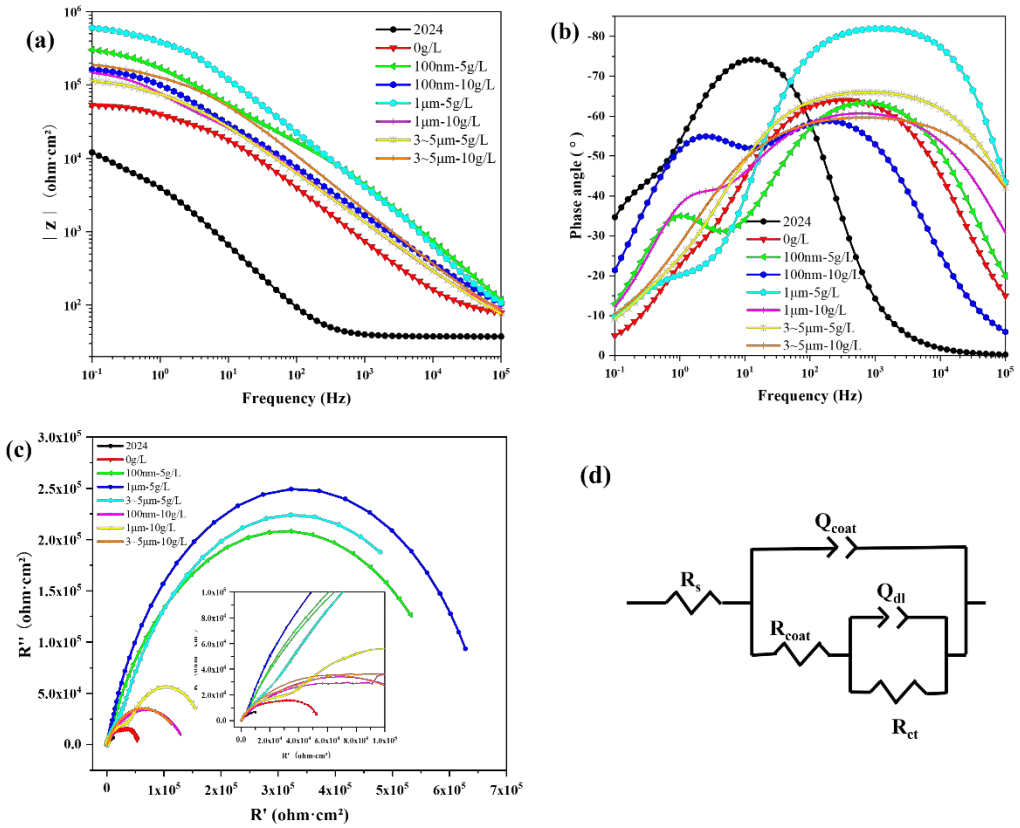

Fig. S2. (a-c) Nyquist and bode plots doped with samples of different particle sizes and concentrations of h-BN; (d) Equivalent circuit for the EIS data.

Table. S2. EIS data fitting results.

Sample	R_s ($Ohm·cm^2$)	Q_{coat} ($Ohm^{-2}·cm^{-2}·S^{-n}$)	n_1	R_{coat}($Ohm·cm^2$)	Q_{dl}	n_2	R_{ct} ($Ohm·cm^2$)
2024	37.37	$3.402×10^{-5}$	0.9141	7106	$1.197×10^{-4}$	0.842	$1.332×10^{4}$
0g/L	15.73	$2.79×10^{-6}$	0.6359	284.2	$1.218×10^{-7}$	1	$5.514×10^{4}$
1μm-5g/L	$7.81×10^{-6}$	$2.54×10^{-7}$	0.7731	9970	$1.041×10^{-7}$	0.8932	$6.637×10^{5}$
1μm-10g/L	134.9	$6.088×10^{-7}$	0.7638	$5.075×10^{4}$	$3.194×10^{-6}$	0.8	$1.241×10^{5}$
100nm-5g/L	77.25	$2.453×10^{-6}$	0.7827	2613	$4.065×10^{-7}$	0.7291	$6.213×10^{5}$
100nm-10g/L	26.27	$9.839×10^{-7}$	0.5838	$1.105×10^{5}$	$1.524×10^{-9}$	0.7687	$2.741×10^{4}$
3~5μm-5g/L	573.8	$7.135×10^{-7}$	0.7442	$8.605×10^{4}$	$5.057×10^{-7}$	0.8637	$5.573×10^{5}$
3~5μm-10g/L	29.29	$1.881×10^{-6}$	0.6825	$5.517×10^{4}$	$8.078×10^{-6}$	0.8	$5.573×10^{4}$

Sample 1μm-5g/L shows the highest impedance (0.1Hz) as shown in Figure S2(a) and the Nyquist plot (Fig. S2c) discloses. The radian of the 1μm-5g/L sample is the largest. The anti-corrosion capability of the samples prepared by adding 5 g/L h-BN is better than that of samples prepared with 10 g/L h-BN. The anti-corrosion capability of the 10 g/L concentration samples is poor but is still slightly better than that of samples without h-BN and better than that of the 2024 substrate. Fig. S2(d) depicts the equivalent circuit, where R_s is the circuit resistance and electrolyte resistance, R_{coat} is the film resistance, R_{ct} is the charge transfer resistance, Q_{coat} is the coating capacitance, and Q_{dl} is the double-layer capacitance. The polarization resistance (R_p) is obtained by summing R_{coat} and R_{ct}. According to Table. S2, the 1μm-5g/L sample has the largest R_p and the best corrosion resistance at 5 g/L concentration. At a concentration of 10 g/L, the 1μm-10g/L sample shows the largest R_p and best corrosion resistance. R_p of the samples prepared at 5 g/L concentrations h-BN with three particle sizes is greater than that of samples prepared with 10 g/L h-BN. Therefore, in a follow-up experiment to explore the effect of h-BN on corrosion resistance, a particle size of 1 μm is selected and the concentration is about 5 g/L.